Direct characterization of the evanescent field in objective-type total internal reflection fluorescence microscopy

CHRISTIAN NIEDERAUER, PHILIPP BLUMHARDT, JONAS MÜCKSCH, MICHAEL HEYMANN, ARMIN LAMBACHER, AND PETRA SCHWILLE[*]

Max Planck Institute of Biochemistry, Am Klopferspitz 18, 82152 Martinsried, Germany
[*]*schwille@biochem.mpg.de*

Abstract: Total internal reflection fluorescence (TIRF) microscopy is a commonly used method for studying fluorescently labeled molecules in close proximity to a surface. Usually, the TIRF axial excitation profile is assumed to be single-exponential with a characteristic penetration depth, governed by the incident angle of the excitation laser beam towards the optical axis. However, in practice, the excitation profile does not only comprise the theoretically predicted single-exponential evanescent field, but also an additional non-evanescent contribution, supposedly caused by scattering within the optical path or optical aberrations. We developed a calibration slide to directly characterize the TIRF excitation field. Our slide features ten height steps ranging from 25 to 550 nanometers, fabricated from a polymer with a refractive index matching that of water. Fluorophores in aqueous solution above the polymer step layers sample the excitation profile at different heights. The obtained excitation profiles confirm the theoretically predicted exponential decay over increasing step heights as well as the presence of a non-evanescent contribution.

References and links

1. C. J. Merrifield, M. E. Feldman, L. Wan, and W. Almers, "Imaging actin and dynamin recruitment during invagination of single clathrin-coated pits," Nat. Cell Biol. **4**, 691–698 (2002).
2. M. Midorikawa and T. Sakaba, "Imaging exocytosis of single synaptic vesicles at a fast CNS presynaptic terminal," Neuron. **88**, 492–498 (2015).
3. M. Oheim, D. Loerke, W. Stühmer, and R. H. Chow, "The last few milliseconds in the life of a secretory granule," Eur. biophysics journal **27**, 83–98 (1998).
4. S. Saffarian and T. Kirchhausen, "Differential evanescence nanometry: Live-cell fluorescence measurements with 10-nm axial resolution on the plasma membrane," Biophys. J. **94**, 2333–2342 (2008).
5. J. A. Steyer, H. Horstmann, and W. Almers, "Transport, docking and exocytosis of single secretory granules in live chromaffin cells," Nature. **388**, 474–478 (1997).
6. S. Barg, M. K. Knowles, X. Chen, M. Midorikawa, and W. Almers, "Syntaxin clusters assemble reversibly at sites of secretory granules in live cells," Proc. Natl. Acad. Sci. **107**, 20804–20809 (2010).
7. A. Brodovitch, L. Limozin, P. Bongrand, and A. Pierres, "Use of TIRF to monitor T-Lymphocyte membrane dynamics with submicrometer and subsecond resolution," Cell. Mol. Bioeng. **8**, 178–186 (2015).
8. M. Poteser, G. Leitinger, E. Pritz, D. Platzer, I. Frischauf, C. Romanin, and K. Groschner, "Live-cell imaging of ER-PM contact architecture by a novel TIRFM approach reveals extension of junctions in response to store-operated Ca^{2+}-entry," Sci. Reports **6**, 35656 (2016).
9. D. J. Williamson, D. M. Owen, J. Rossy, A. Magenau, M. Wehrmann, J. J. Gooding, and K. Gaus, "Pre-existing clusters of the adaptor Lat do not participate in early T cell signaling events," Nat. Immunol. **12**, 655–662 (2011).
10. E. B. Lomakina, G. Marsh, and R. E. Waugh, "Cell surface topography is a regulator of molecular interactions during chemokine-induced neutrophil spreading," Biophys. J. **107**, 1302–1312 (2014).
11. V. T. Chang, R. A. Fernandes, K. A. Ganzinger, S. F. Lee, C. Siebold, J. McColl, P. Jönsson, M. Palayret, K. Harlos, C. H. Coles, E. Y. Jones, Y. Lui, E. Huang, R. J. C. Gilbert, D. Klenerman, A. R. Aricescu, and S. J. Davis, "Initiation of T cell signaling by CD45 segregation at 'close contacts'," Nat. Immunol. **17**, 574–582 (2016).

12. S. A. Hocdé, O. Hyrien, and R. E. Waugh, "Molecular accessibility in relation to cell surface topography and compression against a flat substrate," Biophys. J. **97**, 369–378 (2009).

13. Y. Jung, I. Riven, S. W. Feigelson, E. Kartvelishvily, K. Tohya, M. Miyasaka, R. Alon, and G. Haran, "Three-dimensional localization of T-cell receptors in relation to microvilli using a combination of superresolution microscopies," Proc. Natl. Acad. Sci. **113**, E5916–E5924 (2016).

14. J. Boulanger, C. Gueudry, D. Münch, B. Cinquin, P. Paul-Gilloteaux, S. Bardin, C. Guérin, F. Senger, L. Blanchoin, and J. Salamero, "Fast high-resolution 3D total internal reflection fluorescence microscopy by incidence angle scanning and azimuthal averaging," Proc. Natl. Acad. Sci. **111**, 17164–17169 (2014).

15. B. P. Olveczky, N. Periasamy, and A. S. Verkman, "Mapping fluorophore distributions in three dimensions by quantitative multiple angle-total internal reflection fluorescence microscopy." Biophys. J. **73**, 2836–2847 (1997).

16. M. Cardoso Dos Santos, R. Déturche, C. Vézy, and R. Jaffiol, "Topography of cells revealed by variable-angle total internal reflection fluorescence microscopy," Biophys. J. **111**, 1316–1327 (2016).

17. M. C. Dos Santos, R. Déturche, C. Vézy, and R. Jaffiol, "Axial nanoscale localization by normalized total internal reflection fluorescence microscopy," Opt. Lett. **39**, 869–872 (2014).

18. Y. Fu, P. W. Winter, R. Rojas, V. Wang, M. McAuliffe, and G. H. Patterson, "Axial superresolution via multiangle TIRF microscopy with sequential imaging and photobleaching," Proc. Natl. Acad. Sci. **113**, 4368–4373 (2016).

19. R. Liu, S. Garcia-Manyes, A. Sarkar, C. L. Badilla, and J. M. Fernández, "Mechanical characterization of protein L in the low-force regime by electromagnetic tweezers/evanescent nanometry," Biophys. J. **96**, 3810–3821 (2009).

20. A. Sarkar, R. B. Robertson, and J. M. Fernandez, "Simultaneous atomic force microscope and fluorescence measurements of protein unfolding using a calibrated evanescent wave," Proc. Natl. Acad. Sci. **101**, 12882–12886 (2004).

21. Y. Seol and K. C. Neuman, "Combined magnetic tweezers and micro-mirror total internal reflection fluorescence microscope for single-molecule manipulation and visualization," in *Single Molecule Analysis,* (Humana), Methods in Molecular Biology, pp. 297–316 (2017).

22. M. Tutkus, T. Marciulionis, G. Sasnauskas, and D. Rutkauskas, "DNA-Endonuclease complex dynamics by simultaneous FRET and fluorophore intensity in evanescent field," Biophys. J. **112**, 850–858 (2017).

23. D. Gingell, O. S. Heavens, and J. S. Mellor, "General electromagnetic theory of total internal reflection fluorescence: The quantitative basis for mapping cell-substratum topography," J. cell science **87**, 677–693 (1987).

24. K. N. Fish, "Total internal reflection fluorescence (TIRF) microscopy," Curr. Protoc. Cytom. **50**, 12.18.1–12.18.13 (2009).

25. T. P. Burghardt, "Measuring incidence angle for through-the-objective total internal reflection fluorescence microscopy," J. Biomed. Opt. **17**, 126007–126007 (2012).

26. M. J. Paszek, C. C. DuFort, M. G. Rubashkin, M. W. Davidson, K. S. Thorn, J. T. Liphardt, and V. M. Weaver, "Scanning angle interference microscopy reveals cell dynamics at the nanoscale," Nat. Methods **9**, 825–827 (2012).

27. M. Brunstein, M. Teremetz, K. Hérault, C. Tourain, and M. Oheim, "Eliminating unwanted far-field excitation in objective-type TIRF. Part I. Identifying sources of nonevanescent excitation light," Biophys. J. **106**, 1020–1032 (2014).

28. M. Brunstein, K. Hérault, and M. Oheim, "Eliminating unwanted far-field excitation in objective-type TIRF. Part II. Combined evanescent-wave excitation and supercritical-angle fluorescence detection improves optical sectioning," Biophys. J. **106**, 1044–1056 (2014).

29. A. L. Mattheyses and D. Axelrod, "Direct measurement of the evanescent field profile produced by objective-based total internal reflection fluorescence," J. Biomed. Opt. **11**, 014006 (2006).

30. J. Oreopoulos and C. M. Yip, "Combined scanning probe and total internal reflection fluorescence microscopy," Methods. **46**, 2–10 (2008).

31. J. Steyer and W. Almers, "Tracking single secretory granules in live chromaffin cells by evanescent-field fluorescence microscopy," Biophys. J. **76**, 2262–2271 (1999).

32. R. Fiolka, Y. Belyaev, H. Ewers, and A. Stemmer, "Even illumination in total internal reflection fluorescence microscopy using laser light," Microsc. Res. Tech. **71**, 45–50 (2008).

33. C. Cabriel, N. Bourg, G. Dupuis, and S. Lévêque-Fort, "Aberration-accounting calibration for 3D single-molecule localization microscopy," Opt. Lett. **43**, 174–177 (2018).

34. H. Brutzer, F. W. Schwarz, and R. Seidel, "Scanning evanescent fields using a pointlike light source and a nanomechanical DNA gear," Nano Lett. **12**, 473–478 (2012).

35. S. Ramachandran, D. A. Cohen, A. P. Quist, and R. Lal, "High performance, LED powered, waveguide based total internal reflection microscopy," Sci. Reports **3**, 2133 (2013).

36. E. T. Graves, C. Duboc, J. Fan, F. Stransky, M. Leroux-Coyau, and T. R. Strick, "A dynamic DNA-repair complex observed by correlative single-molecule nanomanipulation and fluorescence," Nat. Struct. & Mol. Biol. **22**, 452–457 (2015).

37. C. Gell, M. Berndt, J. Enderlein, and S. Diez, "TIRF microscopy evanescent field calibration using tilted fluorescent microtubules," J. Microsc. **234**, 38–46 (2009).

38. N. Unno, A. Maeda, S.-i. Satake, T. Tsuji, and J. Taniguchi, "Fabrication of nanostep for total internal reflection fluorescence microscopy to calibrate in water," Microelectron. Eng. **133**, 98–103 (2015).

39. N. Unno, H. Kigami, T. Fujinami, S. Nakata, S.-i. Satake, and J. Taniguchi, "Fabrication of calibration plate for total internal reflection fluorescence microscopy using roll-type liquid transfer imprint lithography," Microelectron. Eng.

180, 86–92 (2017).

40. T. Uchida, F. Yu, M. Nihei, and J. Taniguchi, "Fabrication of antireflection structures on the surface of optical lenses by using a liquid transfer imprint technique," Microelectron. Eng. **153**, 43–47 (2016).

41. D. Toomre and J. Bewersdorf, "A new wave of cellular imaging," Annu. Rev. Cell Dev. Biol. **26**, 285–314 (2010).

42. T. R. Richard, "Material properties of fluoropolymers and perfluoroalkyl-based polymers," in *Fluoropolymers 2: Properties,* G. G. Hougham, K. Johns, and T. Davidson, eds. (Springer US), Topics in Applied Chemistry, pp. 47–67 (1999).

43. Y. Okamoto, F. Mikes, K. Koike, and Y. Koike, "Amorphous fluoropolymers," in *Handbook of Fluoropolymer Science and Technology,* D. W. Smith, S. T. Iacono, and S. S. Iyer, eds. (Wiley), pp. 378–391 (2014).

44. D. Nečas and P. Klapetek, "Gwyddion: An open-source software for SPM data analysis," Cent. Eur. J. Phys. **10**, 181–188 (2012).

45. J. Mücksch, P. Blumhardt, M. T. Strauss, E. P. Petrov, R. Jungmann, and P. Schwille, "Quantifying reversible surface binding via surface-integrated fluorescence correlation spectroscopy," Nano Lett. **18**, 3185–3192 (2018).

46. J. Ries, E. P. Petrov, and P. Schwille, "Total internal reflection fluorescence correlation spectroscopy: Effects of lateral diffusion and surface-generated fluorescence," Biophys. J. **95**, 390–399 (2008).

47. M. F. Paige, E. J. Bjerneld, and W. E. Moerner, "A comparison of through-the-objective total internal reflection microscopy and epifluorescence microscopy for single-molecule fluorescence imaging," Single Mol. **2**, 191–201 (2001).

48. R. C. Deagle, T.-L. E. Wee, and C. M. Brown, "Reproducibility in light microscopy: Maintenance, standards and SOPs," The Int. J. Biochem. & Cell Biol. **89**, 120–124 (2017).

49. N. L. Thompson, T. P. Burghardt, and D. Axelrod, "Measuring surface dynamics of biomolecules by total internal reflection fluorescence with photobleaching recovery or correlation spectroscopy." Biophys. J. **33**, 435–454 (1981).

50. B. Huang, W. Wang, M. Bates, and X. Zhuang, "Three-dimensional super-resolution imaging by stochastic optical reconstruction microscopy," Science. **319**, 810–813 (2008).

51. S. R. P. Pavani, M. A. Thompson, J. S. Biteen, S. J. Lord, N. Liu, R. J. Twieg, R. Piestun, and W. E. Moerner, "Three-dimensional, single-molecule fluorescence imaging beyond the diffraction limit by using a double-helix point spread function," Proc. Natl. Acad. Sci. **106**, 2995–2999 (2009).

52. M. F. Juette, T. J. Gould, M. D. Lessard, M. J. Mlodzianoski, B. S. Nagpure, B. T. Bennett, S. T. Hess, and J. Bewersdorf, "Three-dimensional sub–100 nm resolution fluorescence microscopy of thick samples," Nat. Methods **5**, 527–529 (2008).

53. Y. Deng and J. W. Shaevitz, "Effect of aberration on height calibration in three-dimensional localization-based microscopy and particle tracking," Appl. optics **48**, 1886–1890 (2009).

54. A. S. Backer and W. E. Moerner, "Extending single-molecule microscopy using optical fourier processing," The J. Phys. Chem. B **118**, 8313–8329 (2014).

55. S. Hell, G. Reiner, C. Cremer, and E. H. K. Stelzer, "Aberrations in confocal fluorescence microscopy induced by mismatches in refractive index," J. Microsc. **169**, 391–405 (1993).

56. I. Izeddin, M. E. Beheiry, J. Andilla, D. Ciepielewski, X. Darzacq, and M. Dahan, "PSF shaping using adaptive optics for three-dimensional single-molecule super-resolution imaging and tracking," Opt. Express **20**, 4957–4967 (2012).

57. B. P. Bratton and J. W. Shaevitz, "Simple experimental methods for determining the apparent focal shift in a microscope system," PLOS ONE **10**, e0134616 (2015).

58. Y. Shechtman, L. E. Weiss, A. S. Backer, S. J. Sahl, and W. E. Moerner, "Precise three-dimensional scan-free multiple-particle tracking over large axial ranges with tetrapod point spread functions," Nano Lett. **15**, 4194–4199 (2015).

1. Introduction

Total internal reflection fluorescence (TIRF) microscopy makes use of a rapidly decaying evanescent field at the interface of two media of different refractive indices to selectively excite fluorophores close to the interface, e.g. at the plasma membrane of a cell on a coverslide. The brightness of a fluorophore reflects the local excitation intensity, therefore the axial dependence of the excitation field in TIRF microscopy offers the possibility to infer the z-position of a fluorophore. Observing the position, movement, or distribution of molecules in, or at the cell membrane provides insights into many biological processes, such as endo- and exocytosis [1–6] or cellular signaling [7–11], as well as (super-resolved) structural information [12–18]. However, a precise knowledge of the axial excitation profile is often required to accurately interpret TIRF data [1–22]. Theory predicts a single-exponential decay function for the axial TIRF intensity $I_{exc}(z)$ with a penetration depth d_{ev} [23]:

$$I_{exc}(z) = I_{0,exc} \exp\left(-z/d_{ev}\right) \tag{1}$$

$$d_{\text{ev}} = \frac{\lambda}{4\pi\sqrt{n_1^2 \sin^2\theta - n_2^2}} \qquad (2)$$

with $I_{0,\text{exc}}$ the intensity directly at the interface, n_1 the refractive index of the coverslide and n_2 the refractive index of the sample. Thus, under ideal conditions, the penetration depth of the evanescent field d_{ev} depends only on the incident angle θ towards the optical axis, for given excitation wavelength λ and refractive indices $n_1 > n_2$ of the coverslide and sample, respectively. Therefore, in previous studies, the penetration depth is often calculated based on measurements of the incident angle [6, 12, 17, 24–26]. However, precisely determining the incident angle may be cumbersome and complicates the optical setup. Furthermore, deviations from the theoretical single-exponential profile have been observed in objective-type TIRF microscopy, presumably caused by light scattering in the optical path or optical aberrations [27–30]. Available methods for the direct characterization of the excitation profile, which are in principle sensitive to deviations from the single-exponential profile, (i) are not applicable in typical (aqueous) refractive index environments [15, 29, 31], (ii) potentially alter the evanescent field by introducing a medium with a different refractive index than the sample [14, 31–33], (iii) require modifications of the setup [4, 19–21, 30, 34–36] or (iv) require sophisticated sample preparation [34, 37]. Promising attempts to fabricate a TIRF calibration slide were recently made by Unno et al. [38, 39] who analyzed TIRF emission from different z-positions on a polymer substrate that matches the refractive index of water. However, their imprint lithography patterning process requires advanced cleanroom equipment and the number of available step heights was limited to three [40].

Due to the lack of a fast and simple way to directly characterize the excitation profile particularly for biological applications, potentially valuable information encoded in the z-dependent intensity of the fluorophores is often entirely neglected or used non-quantitatively, limiting the interpretation of TIRF microscopy data [41]. Here, we present a dip-coating based method to fabricate TIRF calibration slides with ten steps that are easy to use, applicable in a water-refractive index environment, have a long shelf-life, and are compatible with standard TIRF microscopes.

2. Methods

2.1. Dip coating

The calibration slides were fabricated by depositing a staircase-like polymer profile onto conventional microscopy coverslides (24 mm x 50 mm, thickness 170 µm ± 5 µm, Paul Marienfeld GmbH & Co. KG, Lauda Königshofen, Germany) [Fig. 1]. The fluoropolymer material, MY-133MC (Mypolymers Ltd., Ness Ziona, Israel), was selected for its refractive index, stated to be 1.330 at a wavelength of 589 nm, closely matching that of water (Mypolymers Ltd., MY-133MC Datasheet 2018). The refractive index was confirmed using a refractometer (AR7 Automatic Refractometer, Reichert Inc., New York, USA) as $n_{\text{measured}} = 1.3292 \pm 0.0004$ (mean and standard deviation of triplicate measurements). The polymer cures upon exposure to ambient humidity, which allows for an easy manufacturing process without the need for (photo-)lithography or cleanroom equipment. Deposition of the polymer was carried out using a custom-built dip coating setup (see Appendix A), which consisted of a motorized precision linear stage (LTM 45-50-HiSM with position control unit PS10-32, OWIS GmbH, Staufen, Germany) set up vertically on an optical breadboard, and a cuvette containing the dip coating solution (Makro-Küvette 6030-OG, Hellma GmbH, Müllheim, Germany). The coverslides were placed into a custom 3D-printed mount on the linear stage.

Initially, the coverslide was coated with an optical cleaning polymer (First Contact, Photonic Cleaning Technologies, Wisconsin, USA), which formed a removable layer on both sides of the coverslide. This layer was stripped off one side and the samples were then dip coated at 1 mm/s with a solution of the polymer MY-133MC, diluted in the fluorosolvent Novec 7500 (3M, Neuss, Germany), leaving a thin layer of polymer on the coverslide [Fig. 1(b)]. The approach is insensitive
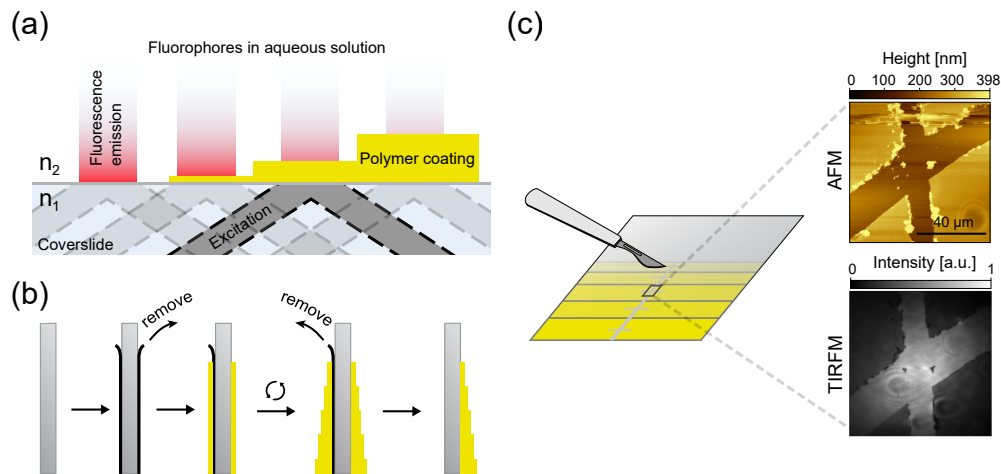
Fig. 1. (a) Calibration slide concept. The TIRF excitation profile is axially sampled by imaging the fluorescent emission of freely diffusing fluorophores in aqueous solution above water refractive index matched polymer step layers of different height on a coverslide.
(b) Fabrication of the calibration slide. A coverslide is coated with a staircase-like profile of a polymer (yellow) with a refractive index matching that of water by repeatedly dip coating the coverslide in a dilute solution of the polymer. Discrete z-steps are obtained by iteratively dip coating the slide while adjusting immersion depth. A protective layer (black) enables the removal of the polymer on one side. (c) Fiducial marks for alignment and measurement of the polymer step height. Fiducials visible in both AFM and TIRF microscopy are created by scratching each polymer step layer with a blade. The scratch also enables the access to the glass surface for measuring the height of the polymer coating with the AFM [Fig. 2].

to small variations of the withdrawal speed, but highest reproducibility was achieved far from the maximum speed of the employed stage (2 mm/s) and slow speeds leading to significant evaporation during withdrawal (0.1 mm/s).

To obtain a multistep slide, dip coating of MY-133MC was repeated several times, at each iteration moving less far into the dip coating solution, thus creating a step-like pattern on the coverslide. After each iteration, the coverslide was left to cure for one hour at ambient temperature and humidity. Since the adhesion of the dip coating solution to the glass surface is different from the adhesion to the already coated surface, the initial dip coating step was performed at a concentration of 1% (v/v), and further steps at a concentration of 3% (v/v). In order to sample the excitation profile at a distance $h \gg d_{ev}$, another step was deposited at a concentration of 10% (v/v) [Fig. 2(d)]. Finally, the remaining First Contact layer was removed, leaving the coverslide patterned on only one side. Final curing was achieved overnight at ambient temperature and humidity.

The cured polymer layers are chemically stable and do not show signs of deterioration over time, or due to washing with commonly used solvents (e.g. isopropyl alcohol, ethanol, purified water), as expected for polymers belonging to the fluoropolymer class [42, 43]. Revisiting the same slide after two months and multiple washing steps yields equivalent height distributions (see Appendix B).

2.2. Characterization of the polymer height

The height of each polymer step relative to the coverslide surface was measured using an atomic force microscope (AFM Nano Wizard 3, JPK Instruments AG, Berlin, Germany). In

order to reference to the original glass surface, the polymer coating was scratched with a blade (Cutfix stainless scalpel #22, Aesculap AG, Tuttlingen, Germany) along the whole length of the coating. AFM height distributions were generated using Gwyddion [44] and fitted by the sum of two Gaussian functions $g(x) = a \cdot \exp\left(-x^2/2\sigma_1^2\right) + b \cdot \exp\left(-(x-\mu)^2/2\sigma_2^2\right)$, with free fitting parameters a and b, μ the height of the coating and σ_1 and σ_2 the respective standard deviation of the height of the glass surface and the coating. The root mean square (RMS) surface roughness of area A is calculated as $S_q = \sqrt{1/A \iint_A z^2(x,y)\,dx\,dy}$ with $z(x,y)$ the vertical AFM tip displacement at point (x,y).

Each step was scratched a second time, perpendicularly, creating fiducial marks to ensure AFM and TIRF imaging at the same position [Fig. 1(c)]. Thorough removal of the coating inside the scratched trench and the absence of damage to the glass surface were confirmed by imaging the beginning of the scratch at the onset of the dip coated area (see Appendix B).

2.3. TIRF imaging

The calibration slides were imaged by a previously introduced custom-built objective-type TIRF setup with focus stabilization, which was constructed around a Nikon Ti-S microscope body (Nikon GmbH, Düsseldorf, Germany) [45]. Total internal reflection of the excitation laser beam was implemented by focusing the laser beam (achromatic lens, $f = 225$ mm, #47-646-INK, Edmund Optics, Karlsruhe, Germany) on the periphery of the back focal plane of the objective (Nikon SR Apo TIRF, 100x magnification, 1.49 numerical aperture). A piezo-electric stage (Q545, Physikalische Instrumente, Karlsruhe, Germany), hereafter referred to as TIR angle stage, was used for translating the excitation beam in the back focal plane in order to adjust the incident angle towards the optical axis (see Appendix C). Optionally, magnification telescopes expanded the excitation laser beam three-fold or ten-fold.

Dip coated calibration slides were prepared for imaging by placing a spacer (22 mm x 40 mm x 0.8 mm SecureSeal Hybridization Chambers, Grace Bio-Labs, Oregon, USA) on the coverslide. The calibration slides were loaded with aqueous solution of 5 µM Alexa Fluor 488 dye (Thermo Fisher Scientific Messtechnik GmbH, Munich, Germany) and imaged at an excitation wavelength of 491 nm (Cobolt Calypso 491 mm, Cobolt AB, Solna, Sweden).

Calibration data were acquired by moving the sample on the motorized xy-stage to the height-characterized areas in the vicinity of the fiducial marks and by recording the respective fluorescence intensity there. The objective was focused on the upper surface of the coverslide and was stabilized at this position throughout the measurement. TIRF images were background corrected by imaging the respective coating steps with pure water, instead of fluorophores in solution, with otherwise unchanged conditions. The contribution of the polymer's autofluorescence to the background signal was shown to be negligible compared to the fluorescence signal level generated by the dye (see Appendix B).

2.4. Data analysis

The axial extent of the objective's detection point spread function is much larger than the penetration depth of the evanescent field, which is typically 60 nm to 200 nm. We determined the detection point spread function from the z-dependent intensity of a fluorescently labeled lipid bilayer, that can be approximated by a Lorentzian function $(s/\pi \cdot (s^2 + z^2)^{-1})$ with a full-width half maximum of $2s = 1.7$ µm. Therefore, the camera detection profile can be assumed constant in the range of the evanescent field. The free fluorophores are excluded from the solid polymer step layers and an integration of the axial excitation along z from the height h of the polymer coating to infinity maintains the theoretical single-exponential excitation profile.

Fluorescence intensity data were analyzed using two different methods. For excitation laser beam diameters considerably smaller than the field of view, a z-dependent spatial separation of
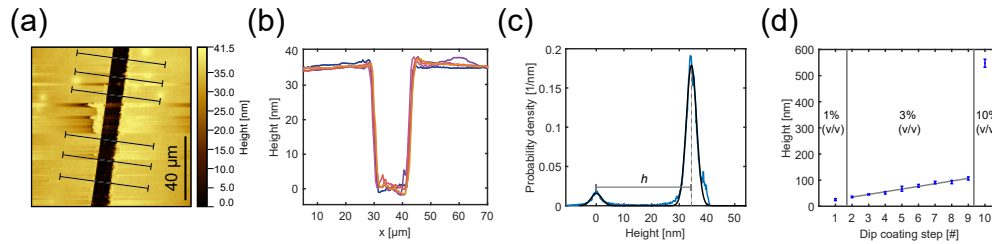
Fig. 2. (a) AFM image of a polymer coating step with a scratch exposing the coverslide surface. The image was leveled by fitting a plane through three points on the exposed coverslide surface and setting it to zero height. (b) Height profiles at positions indicated by the black lines in Fig. 2(a). The height profiles show a consistent mean polymer step height of 34 nm. Each profile is averaged across a width of 6 µm. (c) Probability density compiled from the 256 x 256 height value dataset shown in Fig. 2(a). Two distinct peaks are observable: the smaller peak at 0 nm corresponds to the glass surface exposed by the scratch in the polymer coating. The main peak at 34 nm corresponds to the height of the bulk coating surface. Gaussian fits to the data revealed standard deviations of the height distributions of σ_{glass} = 1.8 nm and $\sigma_{coating}$ = 1.9 nm. A polymer coating RMS surface roughness of 0.35 nm was calculated within a 20 µm x 20 µm area. (d) Height of the polymer coating on glass for ten dip coating iterations using three different concentrations: 1%, 3% and 10% (v/v). Data points correspond to the mean height within an area of 100 µm x 100 µm, measured on three calibration slides coated with the same dip coating procedure. Error bars correspond to the standard deviation of the triplicate measurements.

evanescent and non-evanescent contributions could be observed [Fig. 3(a) and Appendix D]. For each polymer step height, both contributions were fitted by a 2D Gaussian function. Penetration depths were directly obtained by single-exponential fits to the 2D Gaussian amplitudes identified with the evanescent field [Fig. 3(b)]. Alternatively, for arbitrary excitation laser beam diameters, fluorescence intensity data were analyzed pixel by pixel after binning the data [Fig. 4(a)]. Similar to Mattheyses and Axelrod [29], the data were fit using a biexponential function, with contributions from the evanescent field [Eq. 1], and from a non-evanescent contribution, presumably originating from scattering within the optical path and aberrations [27, 29]. Describing the non-evanescent contribution by an exponential function with a long-range decay does not reflect an underlying physical model, but is chosen for mathematical convenience.

3. Results and discussion

3.1. Polymer step heights

Dip coating of the coverslides with a dilute solution of the fluoropolymer reproducibly deposited homogeneous layers in the range of 25 nm to 550 nm. Figure 2(b) shows absolute heights above the glass surface for a polymer step of 34 nm height. Measurements were taken across the whole field of view on several positions along a scratch uncovering the glass surface [Fig. 2(a)]. The coating height within a 100 µm x 100 µm area shows a narrow distribution, fitted by a Gaussian function with a standard deviation of 1.8 nm [Fig. 2(c)]. The RMS surface roughness of the polymer coating was determined as 0.35 nm within an area of interest of 20 µm x 20 µm. Correspondingly, the RMS surface roughness of the uncoated coverglass surface was determined as 0.46 nm. Therefore, height variations within the microscope's field of view (82 µm x 82 µm) as well as the local surface roughness for a given polymer step are negligible. To illustrate the excellent surface properties of the polymer coating, a high-resolution AFM image of a 2 µm x 2 µm area of interest and the corresponding height distribution are shown in Appendix B.

The deposition of a staircase-like polymer profile on a single coverslide was achieved by dip

coating the coverslide repeatedly using different concentrations. Figure 2(d) shows polymer layer heights ranging from 25 nm to 550 nm by employing dip coating solutions of 1%, 3% and 10% (v/v). The polymer layer height for two slides following the same dip coating protocol varied up to 15%. Therefore, the height of every step was still characterized for each slide. Further engineering for a standardization of the production process will allow to relinquish these quality controls.

3.2. Characterization of the excitation profile

Representative TIR images of free Alexa Fluor 488 dye in aqueous solution above polymer step layers of increasing heights are shown in Fig. 3(a). As expected for a TIR excitation profile, the intensity rapidly decreases with increasing height. Accordingly, this decay can be described by an evanescent field with a purely imaginary k-vector, decaying exponentially in axial direction. In addition to the evanescent field contribution, another component is observed decaying over a much larger coating height range. 2D Gaussian fits to the 2D intensity distributions of the two components reveal one spatially fixed contribution (identified as evanescent with a penetration depth matching theoretical predictions), and one contribution spatially separating from the evanescent contribution as the polymer layer heights increase (see Appendix D). The z-dependent separation along one predominant lateral direction, and the intensity varying over a long range compared to the evanescent penetration depth, suggest a non-evanescent character for this contribution. The non-evanescent component is supposedly propagating light with real axial and lateral k-vector components.

Figure 3(b) shows the amplitudes of 2D Gaussian fits to the evanescent and the non-evanescent contribution for various polymer step heights at an incident angle of 71.71° (determined by the lateral displacement of the center of fluorescence excitation upon axially translating the sample; see Appendix C). An exponential fit to the amplitudes of the evanescent contribution yielded a penetration depth of $d_{ev} = 67.3$ nm ± 4.3 nm, closely matching the theoretically expected penetration depth (see section 4 for a more detailed discussion). The amplitudes of 2D Gaussian fits to the non-evanescent contribution are observed to decrease much slower. Consequently, close to the surface, the evanescent excitation dominates, but for distances $h \gg d_{ev}$ above the coverslide, the non-evanescent contribution prevails.

The spatial separation of both components is only observable for excitation beam diameters considerably smaller than the field of view of the microscope. In order to obtain penetration depths for arbitrary lateral illumination profiles, and to potentially resolve spatial variations of the penetration depth within the microscope's field of view, binned fluorescence intensity data of different polymer step heights were analyzed pixel by pixel [Fig. 4(a)]. Magnification telescopes were placed into the optical path to expand the excitation laser beam diameter. Maps of the evanescent field's penetration depth for an incident angle of 71.71° (measured with the lateral displacement method) for laser beams of different diameter are presented in Fig. 4(a) and show similar penetration depths of $d_{ev,1x} = 64.8$ nm ± 2.6 nm, $d_{ev,3x} = 66.7$ nm ± 6.9 nm and $d_{ev,10x} = 64.9$ nm ± 6.0 nm, equally matching the penetration depth of 67.3 nm ± 4.3 nm obtained with the 2D Gaussian fit approach [Fig. 3(b)].

The dependence of the evanescent penetration depth on the angle of incidence of the excitation laser beam was examined by characterizing the TIRF excitation profile for a range of TIR angle stage positions. Additionally, the corresponding incident angles of the laser beam towards the optical axis were determined independently using the lateral displacement method (see Appendix C). Penetration depths obtained with the calibration slide are presented in Fig. 4(b), together with predicted values for the penetration depth, calculated based on incident angle data using equation 2. Direct characterization with the calibration slide reproduced the theoretically expected penetration depths with errors below 10%. A systematic error towards shorter penetration depths may be explained by supercritical angle fluorescence effects, which result in an effective reduction
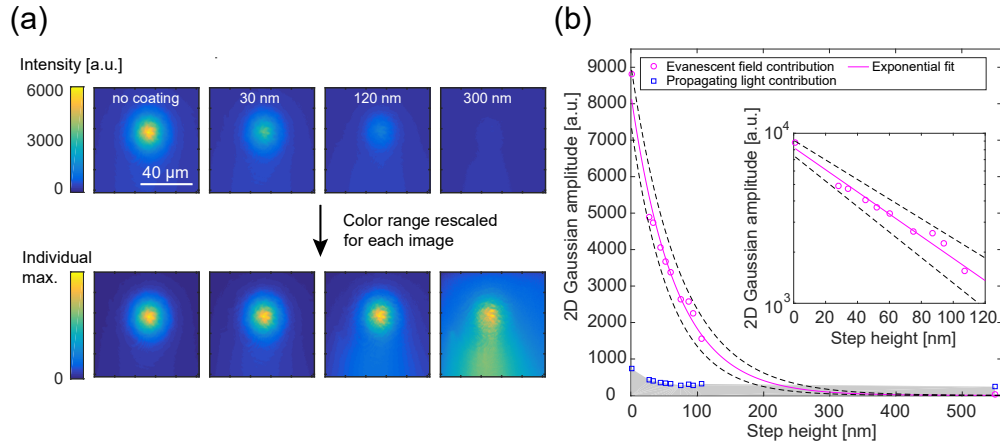
(a)

(b)

Fig. 3. (a) Representative images of free Alexa Fluor 488 dye above polymer step layers of different height. Upper row: the intensity is observed to decrease with increasing step height, as expected for an evanescent field. Lower row: corresponding images with the colormap's range rescaled to each image's individual maximum value reveals a second, putatively non-evanescent contribution. With increasing height, the relative amplitude of the evanescent and non-evanescent contributions shifts towards the non-evanescent part. Images were acquired without a beam expander. (b) Calibration data for a TIR angle stage setting of 2.8 mm (corresponding to an incident angle of the excitation laser beam of 71.71°, as measured with the lateral displacement method). The amplitudes of 2D Gaussian fits to the spatially separating contributions represent the rapidly decaying evanescent part (circles), and the rather constant non-evanescent part (squares). An exponential fit (solid line, with dotted lines representing 95% confidence intervals of the fit parameters) yields an evanescent penetration depth of $d_{ev} = 67.3$ nm ± 4.3 nm. The dataset was acquired using another calibration slide than in panel (a), therefore sampling different heights. Inset: Detail of the data for step heights $h \approx d_{ev}$ as a semi-log plot.

of the evanescent field's penetration depth [46]. Furthermore, it is important to note that the penetration depth calculated from the incident angle strongly depends on the exact values of the refractive indices n_1 and n_2. Refractive index values are often available only for few wavelengths and therefore have to be inter-/extrapolated for the wavelength used in the specific experiment [37]. Theoretically expected penetration depths in Fig. 4(b) were calculated using refractive indices of $n_1 = 1.5297$ (Schott AG, D263 Cover Glass Datasheet) and $n_2 = 1.333$ (Mypolymers Ltd., Study of non-cured MY-133: Refractive index vs. wavelength, 2018).

4. Conclusion

We fabricated and evaluated a calibration slide for the direct and accurate characterization of the TIRF excitation field in an aqueous refractive index environment. The calibration slides were fabricated following a simple and low-cost dip coating approach to deposit polymer step layers with a refractive index matching that of water onto a conventional coverslide. Evanescent penetration depths, obtained with the calibration slide for different incident angles were compared to penetration depths calculated based on the incident angle, measured independently with the lateral displacement method. Penetration depths obtained with both methods were in good agreement, validating our calibration slide as an adequate tool for direct evanescent field characterization in TIRF microscopy. Furthermore, deviations from the idealized single-exponential excitation profile could be observed with the calibration slide and were associated with non-evanescent light, supposedly caused by scattering in the optical path and aberrations [27–29, 47].
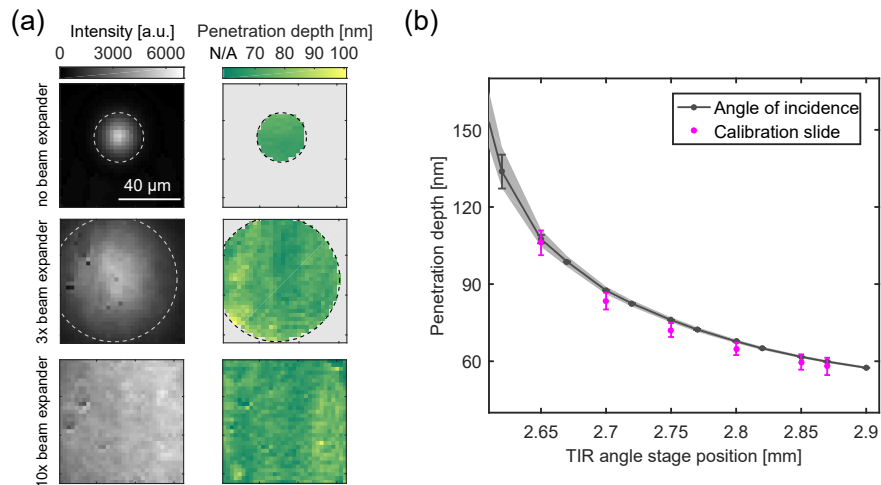
Fig. 4. (a) Illumination profile and evanescent penetration depths for different excitation beam diameters. The fluorescence intensity of free Alexa Fluor 488 for three excitation beam diameters (left column) and the corresponding evanescent penetration depths (right column) as determined with the calibration slide, are shown for a TIR angle stage position of 2.8 mm (corresponding to an incident angle of the excitation laser beam of 71.71°, as measured with the lateral displacement method). Penetration depths were evaluated in the area defined by the $1/e^2$ beam diameter (determined by a 2D Gaussian fit to the lateral illumination profile) with the exterior data assigned as not applicable (N/A) due to the low signal-to-background ratio. Upper row: no beam expander, $d_{ev,1x} = 64.8$ nm ± 2.6 nm, mid row: 3-fold beam expander $d_{ev,3x} = 66.7$ nm ± 6.9 nm, lower row: 10-fold beam expander $d_{ev,10x} = 64.9$ nm ± 6.0 nm. Binning: 32 x 32 pixels (5.12 μm x 5.12 μm). (b) Penetration depths of the evanescent field for a range of TIR angle stage positions, corresponding to different incident angles. Data are given as the mean and standard deviation within the microscope's field of view, obtained in a single calibration run. Theoretically expected penetration depths, calculated based on incident angle data using equation 2, show close agreement with directly measured values using the calibration slide. Data are given as the mean and standard deviation of three independent lateral displacement measurements (see Appendix C) with the shaded area indicating an uncertainty of refractive index values of $\Delta n = 0.0015$. Both datasets were acquired without a beam expander.

Our calibration slide may serve as a tool to routinely check the quality and reproducibility of the evanescent field generated by the multitude of commercial and custom-built TIRF setups [48], thus simplifying interpretation and comparability of acquired data from TIRF microscopes. Furthermore, approaches where the shape of the axial excitation profile is used to infer the axial position of fluorescently labeled molecules [1–13, 19–22], in particular when combined with incident angle scanning [14–18], will benefit from a fast and precise single-slide calibration tool.

Moreover, the precise knowledge of the axial excitation profile offers access to the description of 3D diffusion kinetics in total internal reflection-fluorescence correlation spectroscopy (TIR-FCS) [49].

Apart from the applications in TIRF microscopy, the calibration slide may also assist 3D single-molecule localization microscopy, where the axial localization typically relies on an initial calibration of the point spread function, using immobilized fluorescent beads [50–52]. However, the point spread function of an emitter adhering to the coverslide surface is different from the point spread function of a source deeper in solution [53–55]. This potential error, which otherwise needs to be treated with advanced aberration corrections [53, 56–58], is circumvented by simply

imaging immobilized emitters on the individual polymer step layers of the presented calibration slide. Necessary higher step sizes or a larger total height range are simply achieved by using a more concentrated polymer dip coating solution.

Taken together, we believe that the described tool will be of great help for all researchers frequently requiring simple and low-cost solutions for optical quality control and axial calibration in TIRF and single-molecule localization microscopy.

Appendix

A. Dip coating setup

Figure 5 shows the custom-built setup used for dip coating coverslides with thin polymer layers. A motorized precision linear stage (1; LTM 45-50-HiSM, OWIS GmbH, Staufen, Germany) is mounted vertically on a solid base plate (2). A position control unit (3; PS10-32, OWIS GmbH, Staufen, Germany) drives the stage. Coverslides are placed into a custom 3D-printed mount (4) and dipped into a cuvette (5; Makro-Küvette 6030-OG, Hellma GmbH, Müllheim, Germany) containing the dip coating solution. CAD files of the 3D-printed parts are available upon request.
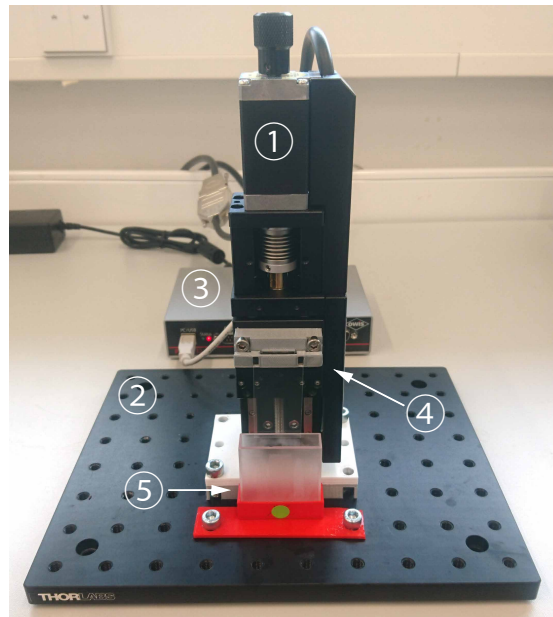
Fig. 5. Dip coating setup. A motorized precision linear stage (1) is mounted vertically on a solid base plate (2). A position control unit (3) drives the stage. Coverslides are placed into a custom 3D-printed mount (4) and dipped into a cuvette (5) containing the dip coating solution.

B. Supplementary studies on polymer properties

Here, we present further studies on the physical properties of the thin polymer layers. Figure 6(a) assesses the shelf-life of the calibration slides. AFM height distributions of the same slide recorded two months apart and with multiple washing steps in between show no change in the polymer layer thickness, with an initial thickness of $45.6\,\text{nm} \pm 2.3\,\text{nm}$, and a revisited slide thickness of $47.6\,\text{nm} \pm 2.1\,\text{nm}$, as determined by the distance of Gauss peak centers and their combined standard deviation. The absence of any signs of deterioration over time, and especially the chemical and mechanical stability against washing the calibration slides with commonly

used solvents (e.g. isopropyl alcohol, ethanol, purified water) suggest a long shelf-life and the reusability of the calibration slides.

Access to the original glass surface for measuring the polymer layer thickness was created by scratching the polymer coating with a scalpel. In order to ensure the integrity of the glass surface, as well as the thorough removal of polymer in the scratched trench, an AFM image of the beginning of the scratch at the transition from coverslide surface to the coating was recorded [Fig. 6(b)]. No signs of damage to the coverslide surface are observed. Furthermore, the complete removal of polymer material is inferred by equal height levels of the uncoated glass surface and the formerly coated surface in the trench. Conclusively, scratching the surface with a scalpel is a reliable method to uncover the glass surface.

Autofluorescence of the polymer was characterized by comparing the fluorescence intensity of a blank coverslide covered with pure water to the fluorescence intensities of a dip coated coverslide with a 200 nm thick polymer coating, covered with pure water, and covered with dye in aqueous solution [Fig. 6(c)]. For the chosen laser settings with a peak irradiance of 15 W/cm^2 at an excitation wavelength of 491 nm), and a concentration of 5 µM Alexa Fluor 488 dye in aqueous solution, additional autofluorescence caused by the polymer coating is negligible compared to the fluorescence emission of the dye in aqueous solution.
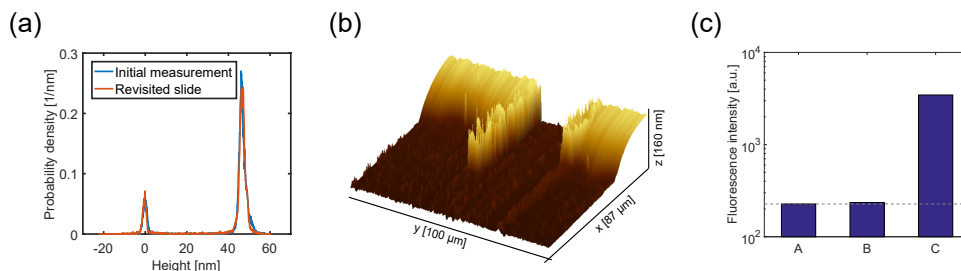
Fig. 6. (a) Shelf-life of the calibration slides. AFM height distributions of the same slide recorded two months apart and with multiple washing steps in between show no change in the polymer layer thickness, with the initial thickness determined as 45.6 nm ± 2.3 nm, and the revisited slide thickness of 47.6 nm ± 2.1 nm (distance of Gauss peak centers ± combined standard deviation). (b) Uncovering of the glass surface by scratching the coating. An AFM image of the beginning of the scratch at the transition from coverslide surface to the coating shows thorough removal of the polymer down to the glass surface. Furthermore, no signs of damage to the coverslide surface are observed. (c) Polymer autofluorescence. Background (dotted line) and (auto-)fluorescence intensities for a blank coverslide covered with pure water (A), and a coverslide with a 200 nm coating covered with pure water (B) and 5 µM Alexa Fluor 488 dye in aqueous solution (C). At a peak irradiance of 15 W/cm^2 at 491 nm and 5 µM Alexa Fluor 488, additional autofluorescence caused by the polymer coating is negligible compared to the dye's fluorescence.

Possible applications of the presented calibration slide may involve (single-molecule) experiments where the probed regions are small compared to the regions being probed in this work. Therefore, a representative high-resolution AFM image of a 2 µm x 2 µm area of the polymer surface, with a pixel size of 15.6 nm x 15.6 nm, and the associated probability density are shown in Fig. 7. A Gaussian fit to the probability density reveals a standard deviation of 0.22 nm around the mean height. The RMS surface roughness is 0.34 nm. Both the local variability of the height, as well as the RMS surface roughness suggest excellent applicability of the calibration slide for experiments where highly-precise positioning in the axial dimension is required.
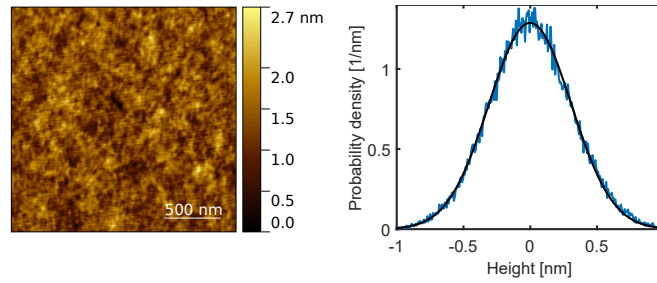
Fig. 7. High-resolution AFM image of the polymer surface. The pixel size of the AFM data is 15.6 nm x 15.6 nm. The probability density of height values around the mean polymer step height is fit with a Gaussian function with a standard deviation of 0.22 nm. The RMS surface roughness is 0.34 nm.

C. Lateral displacement method

The incident angle θ for a given TIR angle stage position x is determined based on a method shown in Fig. 8(a), first presented by T.P. Burghardt [25]. A sample of free 5 µM Alexa Fluor 488 dye (Thermo Fisher Scientific Messtechnik GmbH, Munich, Germany) in aqueous solution is mounted on the objective. A series of images with the sample translated along the z-direction in steps of $\Delta z = 0.1$ µm is acquired ('z-stack'). The large incident angle θ of the excitation beam results in a measurable lateral displacement Δy of the fluorescence excitation spot when the sample is moved axially [Fig. 8(b)]. Lateral displacements Δy_i of the illumination profile are extracted by the displacement of the center position of a 2D Gaussian fit to each image. To ensure reliable and precise fitting, no magnification telescope is used so that the excitation laser beam diameter fits well into the field of view. Figure 8(c) shows the lateral displacement of the centroids in y-direction for different TIR angle stage positions x. A linear fit $f(z) = mz + c$ to the dependence of Δy on Δz directly gives the incident angle via $\theta = \arctan(m)$, as shown in Fig. 9.
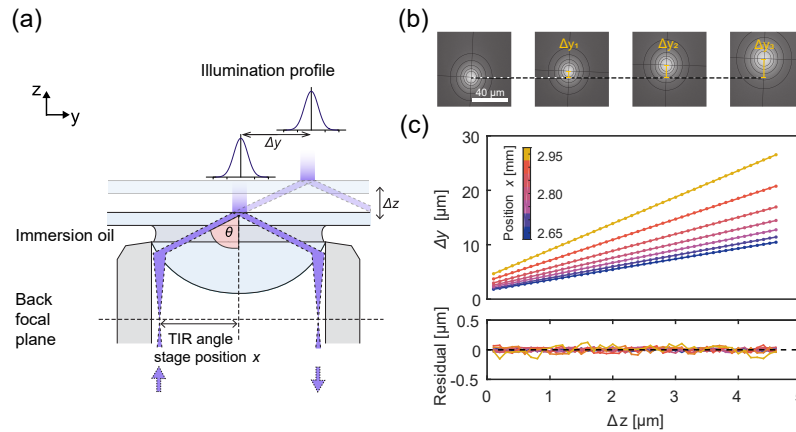

Fig. 8. (a) Lateral displacement method. A sample of free dye is mounted on the objective. The large incident angle θ results in a lateral displacement Δy of the fluorescence excitation spot when the sample is moved axially. (b) Displacement of the illumination profile. Lateral displacements Δy_i of the illumination profile are extracted by 2D Gaussian fits to each image during a z-stack. (c) Linear fit to lateral displacement data. The lateral displacement of the centroids in y-direction during a 4.5 µm z-stack with 0.1 µm step size is shown for different TIR angle stage positions x. Linear fits to the data directly give the incident angles.
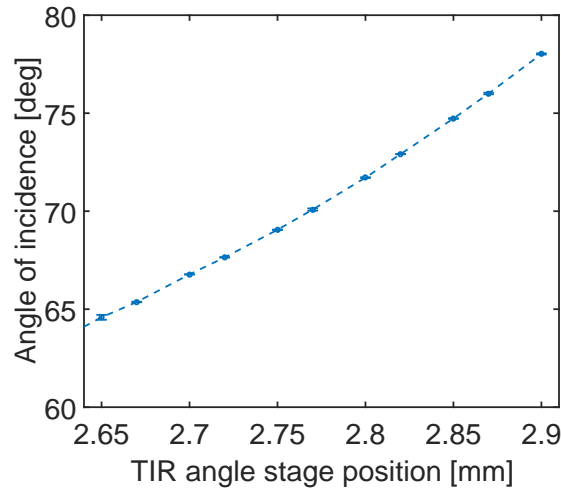
Fig. 9. Look-up-table for relating TIR angle stage positions x to the incident angle θ. Incident angles were determined with the lateral displacement method with an angular precision of 0.1°. Data correspond to mean and standard deviation of triplicate measurements.

D. Supplementary studies on evanescent and non-evanescent contributions

For excitation laser beam diameters small compared to the field of view of the TIRF microscope, a spatial separation of excitation field contributions with increasing polymer layer heights is observed [Fig. 10 (a)]. 2D illumination profiles are fitted with 2D Gaussian functions $g_i(x, y) = A_i \exp\left(-\left[(x - x_{0,i})^2/2\sigma^2_{x,i} + (y - y_{0,i})^2/2\sigma^2_{y,i}\right]\right)$, with coefficients A the amplitude, $x_{0,i}$, $y_{0,i}$ the center positions and $\sigma_{x,i}$, $\sigma_{y,i}$ the x and y widths. The fits are assisted by using the center positions and widths of a single 2D Gaussian fit to the TIRF image of free dye on an uncoated coverslide as the initial fit coefficients for the stationary field contribution. Figures 10 (b − c) show center positions and widths of the two 2D Gaussian fit functions. The center positions and widths of the two 2D Gaussian fits to the illumination profiles separate into two groups, with the one effectively stationary with constant widths for all step heights, and the other one being displaced laterally and becoming wider for increasing step heights. This behavior can be readily explained when identifying the two groups with evanescent and non-evanescent contributions. The evanescent field, with an imaginary k-vector in axial direction and zero lateral components, decays exponentially but otherwise remains unchanged for all sampled heights. Non-evanescent contributions, however, with non-zero real lateral k-vector components predominantly in one direction, produce increasingly laterally displaced fluorescence intensity profiles as the sampled height increases.
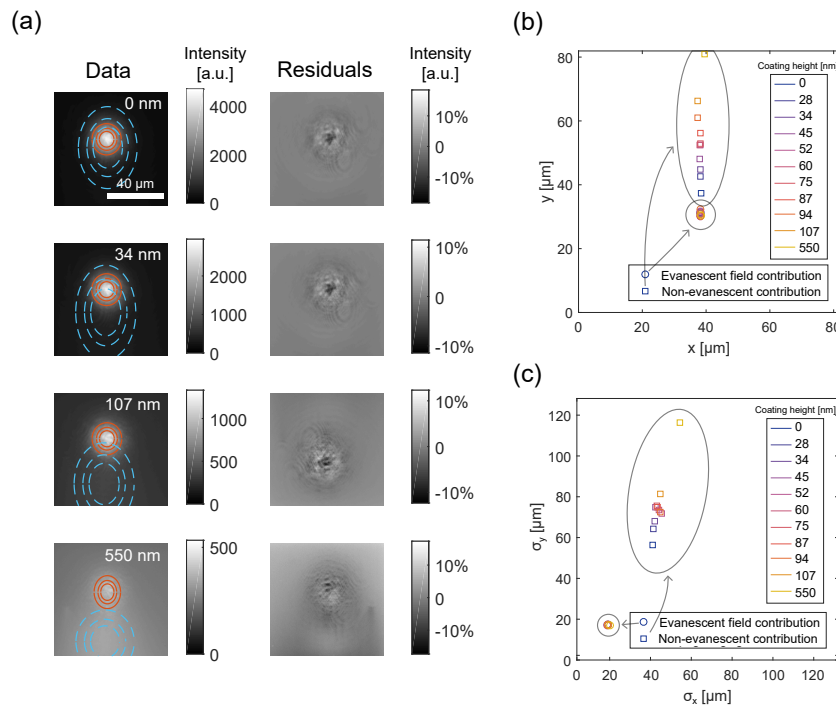
Fig. 10. (a) 2D Gaussians fits of spatially separating excitation field contributions. Left column: TIRF images of free dye above polymer layers of different height show a rapid decay as the step height increases. Illumination profiles were fit with two 2D Gaussian functions (solid orange and dotted blue rings, corresponding to 1/2, 1/4 and 1/8 of the 2D Gaussian fits' width). Right column: Residuals of the 2D Gaussian fits to the experimental data. Mean absolute residuals are below 5% of the respective amplitudes. (b – c) Center positions and widths of the two 2D Gaussian fit profiles. The center positions and widths of the two 2D Gaussian fits to the illumination profiles separate into two groups, with the one effectively stationary with constant widths regardless of the step height, and the other being displaced laterally and becoming wider for increasing step heights, suggesting evanescent and non-evanescent character respectively.